# Structure-based Classification of Tauopathies

**Yang Shi**[#1], **Wenjuan Zhang**[#1], **Yang Yang**[1], **Alexey G. Murzin**[1], **Benjamin Falcon**[1], **Abhay Kotecha**[2], **Mike van Beers**[2], **Airi Tarutani**[3], **Fuyuki Kametani**[3], **Holly J. Garringer**[4], **Ruben Vidal**[4], **Grace I. Hallinan**[4], **Tammaryn Lashley**[5], **Yuko Saito**[6], **Shigeo Murayama**[7], **Mari Yoshida**[8], **Hidetomo Tanaka**[9], **Akiyoshi Kakita**[9], **Takeshi Ikeuchi**[10], **Andrew C. Robinson**[11], **David M.A. Mann**[11], **Gabor G. Kovacs**[12,13], **Tamas Revesz**[5], **Bernardino Ghetti**[4], **Masato Hasegawa**[3], **Michel Goedert**[1,+], **Sjors H.W. Scheres**[1,+]

[1]MRC Laboratory of Molecular Biology, Cambridge, UK

[2]Thermo Fisher Scientific, Eindhoven, The Netherlands

[3]Department of Brain and Neurosciences, Tokyo Metropolitan Institute of Medical Science, Tokyo, Japan

[4]Department of Pathology and Laboratory Medicine, Indiana University School of Medicine, Indianapolis, IN, USA

[5]Department of Neurodegenerative Disease and Queen Square Brain Bank for Neurological Disorders, UCL Queen Square Institute of Neurology, London, UK

[6]Department of Neuropathology, Tokyo Metropolitan Geriatric Hospital and Institute of Gerontology, Tokyo, Japan

[7]Molecular Research Center for Children's Mental Development, United Graduate School of Child Development, University of Osaka, Osaka, Japan

[8]Institute for Medical Science of Aging, Aichi Medical University, Nagakute, Japan

[9]Department of Pathology, Brain Research Institute, Niigata University, Asahimachi, Chuo-ku, Niigata, Japan

[10]Department of Molecular Genetics, Brain Research Institute, Niigata University, Asahimachi, Chuo-ku, Niigata, Japan

Correspondence to: Michel Goedert; Sjors H.W. Scheres.

Correspondence to: mg@mrc-lmb.cam.ac.uk and scheres@mrc-lmb.cam.ac.uk.
[+]These authors jointly supervised this work.

[11]Clinical Sciences Building, University of Manchester, Salford Royal Foundation Trust, Salford, UK

[12]Tanz Centre for Research in Neurodegenerative Diseases and Department of Laboratory Medicine and Pathobiology, University of Toronto, Toronto, Canada

[13]Institute of Neurology, Medical University of Vienna, Vienna, Austria

[#] These authors contributed equally to this work.

## Abstract

Ordered assembly of tau protein into filaments characterizes multiple neurodegenerative diseases, which are called tauopathies. We previously reported that by electron cryo-microscopy (cryo-EM), tau filament structures from Alzheimer's disease (1,2), Pick's disease (3), chronic traumatic encephalopathy (CTE) (4) and corticobasal degeneration (CBD) (5) are distinct. Here we show that the structures of tau filaments from progressive supranuclear palsy (PSP) define a novel three-layered fold. Moreover, the tau filament structures from globular glial tauopathy (GGT) are similar to those from PSP. The tau filament fold of argyrophilic grain disease (AGD) differs from the above and resembles the four-layered CBD fold. The AGD fold is also observed in aging-related tau astrogliopathy (ARTAG). Tau protofilament structures from inherited cases with mutations +3 or +16 in intron 10 of *MAPT*, the microtubule-associated protein tau gene, are also identical to those from AGD, suggesting that relative overproduction of four-repeat tau can give rise to the AGD fold. Finally, tau filament structures from cases of familial British dementia (FBD) and familial Danish dementia (FDD) are the same as those from Alzheimer's disease and primary age-related tauopathy (PART). These findings suggest a hierarchical classification of tauopathies based on their filament folds, which complements clinical diagnosis and neuropathology, and allows identification of new entities, as we show for a case diagnosed as PSP, but with filament structures that are intermediate between those of GGT and PSP.

---

Six tau isoforms are expressed in the adult human brain; three isoforms have three microtubule-binding repeats (3R) and three isoforms have four repeats (4R) (6). Based on the isoforms that constitute the abnormal filaments, tauopathies can be divided into three groups. In PART, Alzheimer's disease, FBD, FDD and CTE, a mixture of 3R+4R tau isoforms is present in the filaments; 3R tau is found in Pick's disease, whereas 4R tau isoforms are present in the filaments of PSP, GGT, CBD, AGD and ARTAG. Dominantly inherited mutations in *MAPT* cause frontotemporal dementias, with filaments made of either 3R, 4R or 3R+4R tau isoforms (7).

We previously showed that Alzheimer's disease, CTE, Pick's disease and CBD are each characterized by a different tau fold (1–5), whereas PART filaments are identical to those from Alzheimer's disease (8). To expand our knowledge of tau filaments in disease, we determined the cryo-EM structures of tau filaments from the brains of individuals with typical and atypical PSP, GGT, AGD, ARTAG, *MAPT* intron 10 mutations +3 and +16, as well as FBD and FDD (Extended Data Figures 1–4, Extended Data Tables 1–2, Supplementary Information Tables 1–3).

## Results

First, we examined filaments from PSP, the most common tauopathy after Alzheimer's disease, and belonging to the group of sporadic frontotemporal lobar degeneration disorders (FTLD-tau). Clinically, typical cases of PSP (Richardson's syndrome; PSP-RS) are characterised by postural instability, supranuclear gaze palsy, behavioural and cognitive impairment, as well as bulbar symptoms (9,10). Neuropathologically, they are defined by abundant subcortical neurofibrillary tangles and neuropil threads, together with tufted astrocytes and oligodendroglial coiled bodies (11,12). Atypical forms of PSP are distinguished by differences in total tau load in specific brain regions (12). We determined structures, with resolutions of up to 2.7 Å, of tau filaments from the frontal cortex and thalamus of three cases of PSP-RS, the putamen and temporal cortex of two cases of PSP with predominant frontal presentation (PSP-F), the frontal cortex of one case with predominant parkinsonism (PSP-P) and the frontal cortex of one case with a predominant presentation of corticobasal syndrome (PSP-CBS).

In PSP-RS, PSP-CBS, PSP-P and PSP-F case 1, we observed tau filaments made of a single protofilament with an ordered core that spans residues 272-381. Although this is essentially the same region as that seen in the CBD core, it adopts a markedly different conformation, which we named the PSP fold (Figure 1b, Extended Data Figure 4a). Tau filament structures were identical between typical and atypical cases of PSP, consistent with the view that the initiating sites of tau pathology are similar in clinical subtypes, which are distinguished by different propagation patterns. When multiple tau seeds are found in a PSP brain (13), this may be indicative of co-pathology.

In the PSP fold, repeats 2-4 (R2-4) form a 3-layer meander turning at the conserved PGGG motifs at the end of each repeat. R3 forms the central layer, which bends at G323 into a near-right angle. Following the outside of this bend, R2 packs against the entirety of R3. The R2-R3 interface contains two small cavities containing additional densities. One, between N279 and G323, and surrounded by hydrophobic side chains, is probably caused by molecules of a predominantly nonpolar nature, whereas the other, next to the salt bridge between K294 and D314, is most likely a solvent molecule. Most of R4 packs against the other side of R3. At the R3-R4 interface, there is a cavity between the positively charged K317, K321 and K340 that contains a bigger additional density, with a volume of ~30 Å$^3$, presumably corresponding to anionic molecules. This cavity is flanked by the negatively charged E338 and E342, reducing the net charge of the cavity to +1 per rung. The rest of the R3-R4 interface is of mixed chemical nature, containing hydrophobic interactions and a salt bridge between K311 and D348. The chain makes another hairpin turn at the PGGG motif of R4, with the C-terminal segment forming a short fourth layer covering the end of R2. On the outside of the PSP core, there are at least six additional densities that were conserved between cases, the most prominent being next to K280-K281 and H362.

We then examined tau filaments from GGT. Like PSP, GGT is a sporadic 4R tauopathy that belongs to the spectrum of FTLD-tau diseases; it is characterized by abundant globular glial tau inclusions (14–16). GGT is divided into three types (GGT-I, GGT-II and GGT-III), depending on the predominant involvement of glial cells in white or grey matter. Structures

of tau filaments from the frontal cortex of previously described cases of GGT-I [case 1 in (17)] and GGT-II [case 1 in (18)], with resolutions of up to 2.9 Å, show a common, previously unknown three-layered protofilament fold, spanning residues 272-379 (Figure 1c, Extended Data Figure 4b). For GGT-I, we observed three filament types: type 1 comprises a single protofilament with the GGT fold; type 2 packs two protofilaments with approximate 21 screw symmetry; type 3 packs two protofilaments in an asymmetrical manner. For GGT-II, we only observed filaments of types 2 and 3. We were unable to solve the structures of tau filaments from the frontal cortex of a previously described case with GGT-III [case 1 in (19)], because of an absence of twist in the imaged filaments.

The GGT fold comprises essentially the same residues as the PSP fold and has a similar three-layered arrangement of R2-4. Again, the chain turns at the PGGG motifs, but each turn has a different conformation compared to its PSP counterpart. Moreover, the C-terminal domain points in the opposite direction and packs against the end of R4 in a hairpin-like structure that is almost identical to the equivalent part of the Pick fold. The only common substructure of the GGT and PSP folds comprises residues 273-285 and 322-330, extending to the additional densities in the small internal cavity between N279 and G323 and outside K280/K281. The cavity at the R3-R4 interface is bigger in the GGT than in the PSP fold and it contains a larger non-proteinaceous density, with a volume of $\sim$50Å$^3$, surrounded by K317, K321 and K340. The cavity's net positive charge is also greater, as E338 forms a salt bridge with K331.

Although the structures of tau filaments from the six cases of typical and atypical PSP described above were identical, we observed a different tau fold for filaments from the temporal cortex of case PSP-F2 (Figure 1d, Extended Data Figure 4c). Since this fold resembled both the GGT and PSP folds, we named it the GGT-PSP-Tau, or GPT, fold. We observed two types of GPT filaments: type 1 filaments comprise a single protofilament; type 2 filaments pack two protofilaments with approximate $2_1$ screw symmetry, creating a large, solvent-filled cavity. Histologically, case PSP-F2 was different from other cases of PSP: it resembled cases with abundant spherical, 4R tau-immunoreactive, basophilic neuronal inclusions in limbic and other brain regions (Extended Data Figure 5) (20–22).

For PSP-F2, we used the same electron microscope that was used previously for structure determination to atomic resolution of an apoferritin test sample (23). Images from this microscope allowed classification into two alternative main chain conformations, one of which led to a reconstruction with a resolution of 1.9 Å (Extended Data Figure 6). This map allowed us to model 19 ordered water molecules per asymmetric unit, but it failed to provide further insights into the nature of the constituent molecules of the additional densities, probably because they did not follow the helical symmetry.

The GPT fold comprises the same residues as the PSP and GGT folds and has a similar three-layered structure. The GPT fold has two large substructures of closely similar conformations compared to the GGT fold: the hairpin formed by residues 356-378, as well as residues 273-294 and 312-346, including the small and large cavities with their associated internal and external additional densities. The relative orientation of the two substructures differs between the GPT and GGT folds, with different conformations of

intervening sequences, in particular in the PGGG turn at the end of R2 and in the N-terminal part of R3 that have similar side chain orientations to PSP. In GPT type 2 filaments, the two symmetric inter-protofilament interfaces resemble the asymmetric interface of GGT type 3 filaments, increasing the overall similarity between GGT and GPT filaments (Extended Data Figure 6).

AGD is another 4R tauopathy belonging to the spectrum of sporadic FTLD-tau diseases (24–28). A defining feature is the presence of argyrophilic grains. Argyrophilic grains are rarely the sole pathological finding in cognitively impaired subjects and are most commonly found together with other tau pathologies, especially neurofibrillary tangles (26). We determined the structures of tau filaments from the nucleus accumbens of two cases of AGD, with resolutions up to 3.4 Å (Figure 2, Extended Data Figure 4d). We observed three types of filaments with a common protofilament core, the AGD fold, that adopts a four-layered ordered structure comprising residues 273-387 (type 1) or 279-381 (type 2), and resembles the CBD fold (5). Like CBD type I and type II filaments, AGD type 1 filaments comprise a single protofilament and AGD type 2 filaments pack two protofilaments with C2 symmetry. We were unable to solve the structure of AGD type 3 filaments to sufficient resolution for atomic modelling, but low-resolution cross-sections suggest an asymmetric packing of two protofilaments with the AGD fold. AGD case 1 also had Alzheimer PHFs and CTE type I filaments; AGD case 2 also had Alzheimer PHFs and SFs (Extended Data Figure 2d).

Residues 293-357 of the AGD fold adopt the same conformation as in the CBD fold. However, the C-terminal segment (368-386) makes different interactions with R2, and the ordered core of the AGD fold is seven amino acids longer than that of the CBD fold. In addition, compared to the CBD cavity, the AGD cavity between R2 and the C-terminal segment is smaller and its net positive charge is less. It also contains a smaller additional density of unknown identity between K294 and K370. In AGD type 2 filaments, the turn at the end of R4, as well as the first and last six residues that form the ordered core of the AGD type 1 filaments, are disordered, and the termini point in a different direction compared to the AGD type 1 filaments.

Histologically, PSP-RS case 3 had also features of AGD, in particular the presence of argyrophilic grains in the entorhinal cortex (Extended Data Figure 7). Consistent with this, besides filaments with the PSP fold in thalamus, we also observed filaments of AGD type 2 and AGD type 3, as well as a minority of Alzheimer PHFs and SFs, in the entorhinal cortex from PSP-RS case 3 (Extended Data Figure 2e). By immunoblotting, the pattern of C-terminally truncated tau bands was like that of PSP in thalamus and like that of CBD in entorhinal cortex (Extended Data Figure 8). Thus, this case had concomitant PSP and AGD, as has been reported for other cases of PSP (26).

Astroglial 4R tau pathology in aging has been increasingly recognized; these cases have been subsumed under the umbrella term of ARTAG (29). Like AGD, ARTAG usually coexists with other pathologies. Structures of the majority species of tau filaments from the hippocampus of a case of ARTAG (30) were identical to AGD type 2 and type 3 filaments. Alzheimer PHFs and SFs were also observed (Extended Data Figure 2f).

Unlike the sporadic diseases described above, mutations +3 and +16 in intron 10 of *MAPT* give rise to a 4R tauopathy that belongs to the spectrum of inherited FTLD-tau (31–34). It is characterized by abundant filamentous tau inclusions in nerve cells and glial cells. Argyrophilic grains are present in entorhinal cortex, hippocampus and frontal cortex. Structures of tau filaments from the frontal cortex of two cases with the +3 mutation and one case with the +16 mutation all showed the AGD fold (Extended Data Figure 2g).

The differences between the structures of tau filaments from 4R tauopathies are consistent with results from immunoblots of sarkosyl-insoluble tau (Extended Data Figure 8). In PSP, CBD, GGT, AGD, ARTAG and *MAPT* intron 10 +3 and +16 mutation cases, tau bands of 64 and 68 kDa were in evidence, indicating the presence of full-length 4R tau. As reported previously (35–37), a strong C-terminal tau band of 33 kDa was also found in PSP and GGT, whereas a strong tau doublet of 37 kDa was seen in CBD, AGD and cases with mutation +16. The 37 kDa bands were also characteristic of ARTAG and cases with mutation +3. The 33 and 37 kDa bands correspond to N-terminally truncated tau at, or near, residues 186-187 and 168-169, respectively. Assembled full-length tau is probably cleaved in the fuzzy coat, with the size differences between the 33 and 37 kDa bands possibly resulting from different arrangements of the ends of the structured cores.

Whereas all diseases described above are 4R tauopathies, we also determined structures of tau filaments from two inherited types of 3R+4R tauopathies. FBD and FDD are caused by mutations in the integral membrane protein 2B gene (*ITM2B*) and are characterized by many extracellular inclusions of British amyloid (ABri) and Danish amyloid (ADan) that are associated with abundant tau-positive neurofibrillary tangles, neuropil threads and dystrophic neurites (38–41). Structures of tau filaments from the hippocampus of a previously described case of FBD (40) and the temporal cortex of a case of FDD (Extended Data Figure 2h) are identical to the PHFs that we previously observed for PART and Alzheimer's disease (1,2,8). The hippocampus from the case of FBD also contained Alzheimer SFs, as well as CTE type I tau filaments, possibly as a result of head trauma.

## Discussion

Clinical features are used to distinguish tauopathies. This is complemented and extended by *post-mortem* neuropathological examination. We now add a third layer of knowledge in the characterisation of these diseases. The cryo-EM structures presented here, together with those described previously (1–5,8), provide an overarching perspective that suggests a hierarchical classification of tauopathies based on their filament folds (Figure 3). We previously postulated that distinct conformers of filamentous tau define different tauopathies (5). This observation still holds. We now also show that some tauopathies share the same fold, and that multiple levels of similarity exist between folds.

The first level of classification is based on the extent of the ordered cores, and coincides with the isoform compositions of tau inclusions in the corresponding diseases. All known tau folds from human diseases have a common ordered core region that comprises R3 and R4, as well as 10-13 amino acids of the C-terminal domain. However, the folds differ in their N-terminal extensions. The Alzheimer and CTE folds, which represent 3R+4R tauopathies,

comprise only one or two amino acids from the C-termini of R1 and R2. The Pick fold, representing the only 3R tauopathy with known filament structures, comprises more than half of R1. Folds observed for 4R tauopathies comprise all of R2 and one or two residues of R1. As we previously observed for the CBD fold, incorporation of 3R tau isoforms is incompatible with the PSP, GPT, GGT and AGD folds, which agrees with the observation that only 4R tau isoforms assemble in these diseases. The presence of N279 from R2 in the fuzzy coat of the Alzheimer fold may explain why this residue is deamidated in tau assemblies from Alzheimer's disease, but not from PSP or CBD (42)

At a second level, for the 3R+4R tauopathies, the CTE fold is distinct from the Alzheimer fold. However, whereas Alzheimer's disease, FBD and FDD are distinct diseases that are characterized by different symptoms and/or neuropathology, they contain tau filaments with the Alzheimer fold. As exemplified by PART, which may be part of Alzheimer's disease (43), the Alzheimer tau fold can form in the absence of Aβ deposits. By contrast, in cases of Alzheimer's disease, FBD and FDD, the presence of extracellular amyloid deposits is accompanied by abundant intraneuronal tau inclusions with the Alzheimer fold. The Alzheimer fold has also recently been described in cases of prion disease with mutations Q160X and F198S in the *PRNP* gene, which are characterized by prion protein amyloid deposits and abundant 3R+4R tau inclusions (44).

Also at a second level, the 4R tauopathies are divided into two classes. The PSP, GPT and GGT folds comprise three-layered core regions, with R2 and R4 packing on either side of R3, whereas the packing of the C-terminal domain against part of R2 provides a fourth layer in the CBD and AGD folds. The division of 4R tauopathies based on three-layered and four-layered folds agrees with observations on post-translational modifications, which showed similarities between PSP and GGT, and between CBD and cases with mutation +16 in intron 10 of *MAPT* (45). A third level of classification for 4R tauopathies is provided by differences at the residue level between the three- and four-layered folds.

The AGD fold is also found in ARTAG, consistent with the presence of granular/fuzzy astrocytes in grey matter in both conditions. AGD and ARTAG can develop with age and coexist in a given human brain with the Alzheimer tau fold. The AGD fold also makes up the tau filaments found in cases with intron 10 mutations +3 and +16 of *MAPT*, consistent with the presence of argyrophilic grains in cases with the +3 mutation (Extended Data Figure 7). Assembled tau in AGD has been reported to lack acetylation (46). Features resembling AGD have also been described in cases of frontotemporal dementia caused by exon 10 mutations S305I and S305S in *MAPT* (47,48). These exonic and all known mutations in intron 10 destabilise the tau exon 10 splicing regulatory element RNA, resulting in a relative overproduction of 4R tau and the formation of 4R tau filaments (49). These filaments may have the AGD fold in common.

We present the first structures of tau filaments from cases with *MAPT* mutations. They form following the relative overproduction of 4R tau. Other *MAPT* mutations cause the assembly of mutant tau, without overproduction (7). Knowing the structures of tau filaments from cases with mutations at residue P301 (32,50–52) will be particularly important, since

they have been used to produce the most widely used mouse models of human tauopathies (53,54). It will be interesting to compare the tau folds from mouse and human brains.

It is remarkable how well neuropathologically confirmed diagnoses correlate with particular tau folds. For instance, PSP and CBD have been grouped as clinically similar, but neuropathologically distinct 4R tauopathies (55). Their tau filament folds belong to different classes, confirming that they are separate disease entities. Prior to its definition, some cases of GGT were diagnosed as atypical PSP (56). Our observations that the tau filaments from GGT-I and GGT-II are distinct from those of PSP support the definition of GGT as a separate neuropathological entity. Moreover, the observation that tau filaments from GGT-III do not twist suggests that GGT-III itself may be a different disease from GGT-I and GGT-II. Likewise, the observation that the structures of tau filaments from PSP-F case 2 are different from those of PSP and GGT suggests that this individual may have suffered from a distinct disease. Histologically, this case was also different from typical and atypical PSP, with abundant spherical, 4R tau-immunoreactive, basophilic neuronal inclusions in limbic and other brain regions. We therefore name this disease Limbic-predominant Neuronal inclusion body 4R Tauopathy (LNT). Additional cases of LNT remain to be identified. It will be interesting to see if other tau folds exist that are intermediate between those of PSP and GGT.

The molecular mechanism that underlie tauopathies remain unknown. The presence of a specific tau fold in a given disease is consistent with its formation in a small number of brain cells, followed by the prion-like like spreading of tau inclusions (57). This may underlie the temporospatial staging of disease (12,27). Knowledge of the tau folds in the different diseases provides a new framework for studying tauopathies that will lead to a better understanding of disease pathogenesis. At a diagnostic level, the current findings will inform ongoing efforts to develop more specific and sensitive tau biomarkers.

## Methods

No statistical methods were used to predetermine sample size. The experiments were not randomized and investigators were not blinded to allocation during experiments and outcome assessment.

### Clinical history and neuropathology

We determined the cryo-EM structures of tau filaments from the brains of seven individuals with PSP, one individual with GGT-I, one individual with GGT-II, two individuals with AGD, one individual with ARTAG, two individuals with mutation +3 in intron 10 of *MAPT*, one individual with mutation +16 in intron 10 of *MAPT*, one individual with FBD and one individual with FDD. *MAPT* was sequenced in all cases. With the exception of the cases with +3 and +16 mutations, the sequences of *MAPT* exons and adjacent introns were wild-type. Since the *H2 MAPT* haplotype is of Caucasian origin (58) and many individuals were Japanese, we did not systematically determine *MAPT* haplotypes. PSP-RS case 1 was in an 83-year-old man who died with a neuropathologically confirmed diagnosis following a 4-year history of postural instability, supranuclear gaze palsy and cognitive impairment. Microscopic features showed degeneration of pallidum, tegmentum

and dentate nucleus of the cerebellum. Abundant 4R tau-positive tangles, neuropil threads, tufted astrocytes and coiled bodies were in evidence. PSP-RS case 2 was in a 70-year-old man who died with a neuropathologically confirmed diagnosis following a 7-year history of postural instability, supranuclear gaze palsy and cognitive impairment. Magnetic resonance imaging (MRI) of the brain showed the hummingbird sign, probably reflecting a severe midbrain atrophy. PSP-RS case 3 was in a 74-year-old man who died following a 5-year history of postural instability, cognitive dysfunction and bulbar symptoms. Neuronal loss and gliosis, as well as abundant 4R tau-immunoreactive neuronal and glial tau inclusions were present in thalamus, subthalamic nucleus, cerebellum, midbrain, pons and medulla; 4R tau-immunoreactive argyrophilic grains were in evidence in entorhinal cortex and hippocampus. The neuropathological diagnosis was PSP + AGD. PSP-F case 1 was in a 62-year-old man who died with a neuropathologically confirmed diagnosis following an 11-year history of behavioural-variant FTD, postural instability and bulbar symptoms. Abundant neuronal and glial 4R tau inclusions were present in cortical and, especially, subcortical areas. Basal ganglia, thalamus and brainstem were severely affected. PSP-F case 2 was in a 66-year-old woman who died with FTD and parkinsonism. Abundant neuronal and glial 4R tau inclusions were present in cortical and subcortical areas. In limbic areas and other brain regions, abundant spherical, 4R tau-immunoreactive, basophilic and Gallyas silver-positive neuronal inclusions were present, together with globular glial tau inclusions. PSP-P was in a 63-year-old man who died with a neuropathologically confirmed diagnosis following a 9-year history of akinetic-rigid parkinsonism, postural instability and cognitive impairment. Brain MRI showed progressive frontal atrophy and mild midbrain atrophy. Neuronal loss was more marked in the substantia nigra than in the pallidum, tegmentum and dentate nucleus of the cerebellum. Abundant neuronal and glial 4R tau pathology was widespread. PSP-CBS was in an 88-year-old woman with a neuropathologically confirmed diagnosis following a 9-year history of corticobasal syndrome, cerebellar ataxia and cognitive impairment. Abundant neuronal and glial 4R tau inclusions were present in cerebral cortex, from the precentral gyrus to the operculum. GGT-I was in a 77-year-old woman with a neuropathologically confirmed diagnosis following a 3-year history of falls, bradykinesia and cognitive impairment. The clinical diagnosis was behavioural-variant FTD with an atypical parkinsonian disorder (17). Neuropathologically, severe anterior frontal and temporal cortical nerve cell loss and severe tau deposition in cerebral cortex and subcortical white matter were in evidence. Abundant neuronal, as well as globular oligodendroglial and astrocytic 4R tau inclusions, were present. GGT-II was in a 76-year-old woman with a neuropathologically confirmed diagnosis following a 5-year history of asymmetric pyramidal signs, diffuse muscle atrophy and dysarthria (18). Severe neuronal loss was present in the motor cortex, with an almost complete loss of Betz cells. Abundant 4R tau neuronal cytoplasmic inclusions, globular oligodendroglial inclusions, coiled bodies and neuropil threads were in evidence. Only a small number of globular astroglial inclusions was seen in the affected cerebral cortex. GGT-III was in a 62-year-old man with a neuropathologically confirmed diagnosis following a 4-year history of parkinsonism, motor signs and dementia (19). Loss of anterior horn cells and degeneration of the corticospinal tract were in evidence. Abundant 4R tau neuronal and globular oligodendroglial and astroglial inclusions were present. Tau filament structures were determined from the nucleus accumbens of two cases of AGD with a predominantly

neuronal 4R tau pathology. The first case was in a 90-year-old man with a 6-year history of memory loss and behavioural changes. By imaging, diffuse atrophy of the medial temporal lobe was observed. At autopsy, a chronic subdural hematoma was present on the right side, supporting the possibility of a previous head injury and consistent with the presence of CTE type I tau filaments. However, there was no history of head trauma. Nerve cell loss and numerous tau-immunoreactive argyrophilic grains were observed in entorhinal cortex, hippocampus and amygdala. Some tau-immunoreactive coiled bodies and bush-like astrocytes were also present. The second case of AGD was in an 85-year-old man with a 3-year history of postural instability and memory loss. At autopsy, atrophy of hippocampus, amygdaloid nucleus and parahippocampal gyrus was present. Abundant 4R tau-immunoreactive argyrophilic grains were in evidence, with some coiled bodies and bush-like astrocytes. ARTAG was identified in an 85-year-old woman with a 1-year history of cancer and depression (30). At autopsy, she had prominent ARTAG (subpial, subependymal, grey matter, white matter and perivascular). A heterozygous mutation at position +3 in intron 10 of *MAPT* was identified in two patients with dementia and a family history of multiple system tauopathy with presenile dementia (MSTD). The first individual was a 54-year-old woman who died following a 7-year history of disinhibition, anxiety and cognitive impairment. The second individual with a +3 mutation in intron 10 of *MAPT* was a 63-year-old woman who died following an 8-year history of dementia with a severe amnestic component. In both individuals, nerve cell loss and gliosis were severe in neocortex, amygdala, entorhinal cortex, hippocampus, basal ganglia, subthalamic nucleus, midbrain and brainstem. Widespread silver-positive neuronal, oligodendroglial and astrocytic 4R tau inclusions were in evidence. A mutation at position +16 in intron 10 of *MAPT* was identified in a 53-year-old man with a 7-year history of behavioural-variant FTD. This subject had a family history of FTD, consistent with dominant inheritance. Abundant 4R tau neuronal and glial cell inclusions were in evidence. Some glial cell inclusions resembled astrocytic plaques. FBD (T to A mutation, removing the stop codon in *ITM2B)* was in a 68-year-old woman with an 11-year history of ataxia and progressive cognitive decline. Her speech became slurred and she experienced problems with swallowing. A brother and two uncles had similar symptoms. As reported previously [case 5 in (40)], neuropathological findings included degeneration of the hemispheric white matter, parenchymal and blood vessel deposits of ABri amyloid, as well as widespread neurofibrillary pathology. This patient had a serious bicycle accident, probably as a result of ataxia, which may explain the presence of CTE type I filaments. FDD (decamer duplication between codons 265 and 266 of *ITM2B*) was in a 52-year-old man from generation V of a previously described kindred (41). He developed cataracts aged 21 and had severe hearing loss, nystagmus and ataxia aged 38. Neuropathological examination showed similar findings as in FBD, with the difference that ADan, which differs from ABri amyloid in its 12 C-terminal amino acids, formed mostly thioflavin S-negative deposits.

## Whole exome sequencing

Target enrichment made use of the SureSelectTX human all-exon library (V6, 58 mega base pairs; Agilent) and high-throughput sequencing was carried out using a HiSeq4,000 (2x75-base-pair paired-end configuration; Illumina). Bioinformatics analyses were performed as described (59)

## Extraction of tau filaments

For cryo-EM, sarkosyl-insoluble material was extracted from frontal cortex (PSP-RS1, PSP-RS2, PSP-P, PSP-CBS, GGT-I, GGT-II, GGT-III, +3 case 1, +3 case 2, +16), temporal cortex (PSP-F2, FDD), entorhinal cortex (PSP-RS3), hippocampus (FBD, ARTAG), putamen (PSP-F1), thalamus (PSP-RS3) and nucleus accumbens (AGD cases 1 and 2), essentially as described (36). Briefly, tissues were homogenized in 20 volumes (v/w) extraction buffer consisting of 10 mM Tris-HCl, pH 7.5, 0.8 M NaCl, 10% sucrose and 1 mM EGTA. Homogenates were brought to 2% sarkosyl and incubated for 30 min. at 37°C. Subsequent steps were carried out at 4° C. For PSP-RS case 1, PSP-RS case 2, PSP-CBS, PSP-P, GGT-II, GGT-III, AGD case 1, AGD case 2, +3 case 1, +3 case 2, +16 case, following a 10 min. centrifugation at 20,000 g, the supernatants were spun at 100,000 g for 20 min. For the rest of the cases, the supernatants from a 10 min. centrifugation at 7,000 g were spun at 100,000 g for 60 min. The pellets were resuspended in 700 μl/g extraction buffer and centrifuged at 9,500 g for 10 min. For PSP-RS case 1, PSP-RS case 2, PSP-CBS, PSP-P, GGT-II, GGT-III, AGD case 1, AGD case 2, and +16 case, the supernatants were diluted 3-fold in 50 mM Tris-HCl, pH 7.5, containing 0.15 M NaCl, 10% sucrose and 0.2% sarkosyl and spun at 166,000 g for 30 min. For the other cases, the supernatants were spun at 100,000 g for 60 min., the pellets resuspended in 700 μl/g extraction buffer and centrifuged at 9,800 g. The supernatants were then spun at 100,000 g for 60 min. Sarkosyl-insoluble pellets were resuspended in 25 μl/g of 20 mM Tris-HCl, pH 7.4, 100 mM NaCl and used for cryo-EM. We previously showed that sarkosyl does not influence the Alzheimer tau fold (8).

## Immunoblotting, histology and silver staining

Immunoblotting was carried out as described (36). Samples were resolved using 4-20% Tris-glycine gels (Novex) and antibody T46 was used at 1:2,000. Histology and immunohistochemistry were carried out as described (60). Brain sections were 8 μm thick and were counterstained with haematoxylin. Primary antibodies were: RD3 (1:1,000); RD4 (1:1,000); AT8 (1:300). Sections were silver-impreganated using the method of Gallyas-Braak (61).

## Electron cryo-microscopy

Extracted tau filaments were centrifuged at 3,000 g for 60 s, before being applied to glow-discharged holey carbon grids (Quantifoil Au R1.2/1.3, 300 mesh) and plunge-frozen in liquid ethane using a Thermo Fisher Vitrobot Mark IV. Images for PSP-F case 2 were acquired on a 300 keV Thermo Fisher Titan Krios G4 microscope, described previously (23), which was equipped with a cold field-emission gun, a Selectrix X energy filter, and a Falcon-IV detector. The energy filter was operated with a slit width of 10 eV. Images were recorded at a total dose of 50 e$^-$/Å$^2$ using aberration-free image shift (AFIS) as incorporated within the Thermo Fisher EPU software at a throughput of 300 images/h in EER format (62). All other data sets were acquired using EPU software on Thermo Fisher Titan Krios microscopes with either a Gatan K2 or K3 detector, using a GIF-quantum energy filter (Gatan) with a slit width of 20 eV to remove inelastically scattered electrons. All data sets were collected in counting mode, except the +3 case 1 and the GGT-III case, which were collected in super-resolution mode. Further details are given in Extended Data Table 1.

### Helical reconstruction

Movie frames were gain-corrected, aligned, dose-weighted and then summed into a single micrograph using RELION's own motion correction program (63). The micrographs were used to estimate the contrast transfer function (CTF) using CTFFIND-4.1 (64). All subsequent image-processing steps were performed using helical reconstruction methods in RELION (65,66). The filaments from PSP-F2, FBD and FDD were picked by crYOLO (67); the rest of the filaments were selected manually in the micrographs. For +3 and +16 cases, filaments of different types were picked separately; for the other data sets different filament types were separated based on the appearance of 2D class averages. For all data sets, reference-free 2D classification was performed to select suitable segments for further processing. Initial 3D reference models were generated *de novo* from the 2D class averages using an estimated rise of 4.75 Å and helical twists according to the observed cross-over distances of the filaments in the micrographs (68) for all data sets, except those from thalamus of PSP-RS case 3, PSP-P, PSP-F case 1, GGT-II, AGD case 2 and ARTAG. Combinations of 3D auto-refinements and 3D classifications were then used to select the best segments for each structure. For all data sets, Bayesian polishing and CTF refinement (69) were performed to further increase the resolution of the reconstructions. For PSP-F case 2, temporal drift in the beam tilt was corrected by grouping every 8,000 consecutively collected segments into separate optics groups before CTF refinement. Final reconstructions were sharpened using the standard post-processing procedures in RELION, and overall final resolutions were estimated from Fourier shell correlations at 0.143 between the two independently refined half-maps, using phase-randomisation to correct for convolution effects of a generous, soft-edged solvent mask (70). Further details of data acquisition and processing are given in Extended Data Table 1 and Supplementary Information Tables 1–3.

### Model building and refinement

Where multiple structures from different cases were obtained, atomic models were only built and refined in the best available maps. For the PSP structure, this was PSP-RS case 1; for the GGT structures, this was GGT-I; for the GPT structures this was PSP-F case 2; for the AGD type 1 filament, this was AGD case 1; for the AGD type 2 filament, this was +16. Atomic models were built manually using COOT (71). Side chain clashes were detected using MOLPROBITY (72) and corrected by iterative cycles of real-space refinement in COOT and Fourier-space refinement in REFMAC (73) and/or real-space refinement in PHENIX (74). For each refined structure, separate model refinements were performed against a single half-map, and the resulting model was compared to the other half-map to confirm the absence of overfitting (Extended Data Figure 3). Figures were prepared using ChimeraX (75) and PyMOL (Schrödinger, LLC). Statistics for the final models are shown in Extended Data Table 1.

## Extended Data
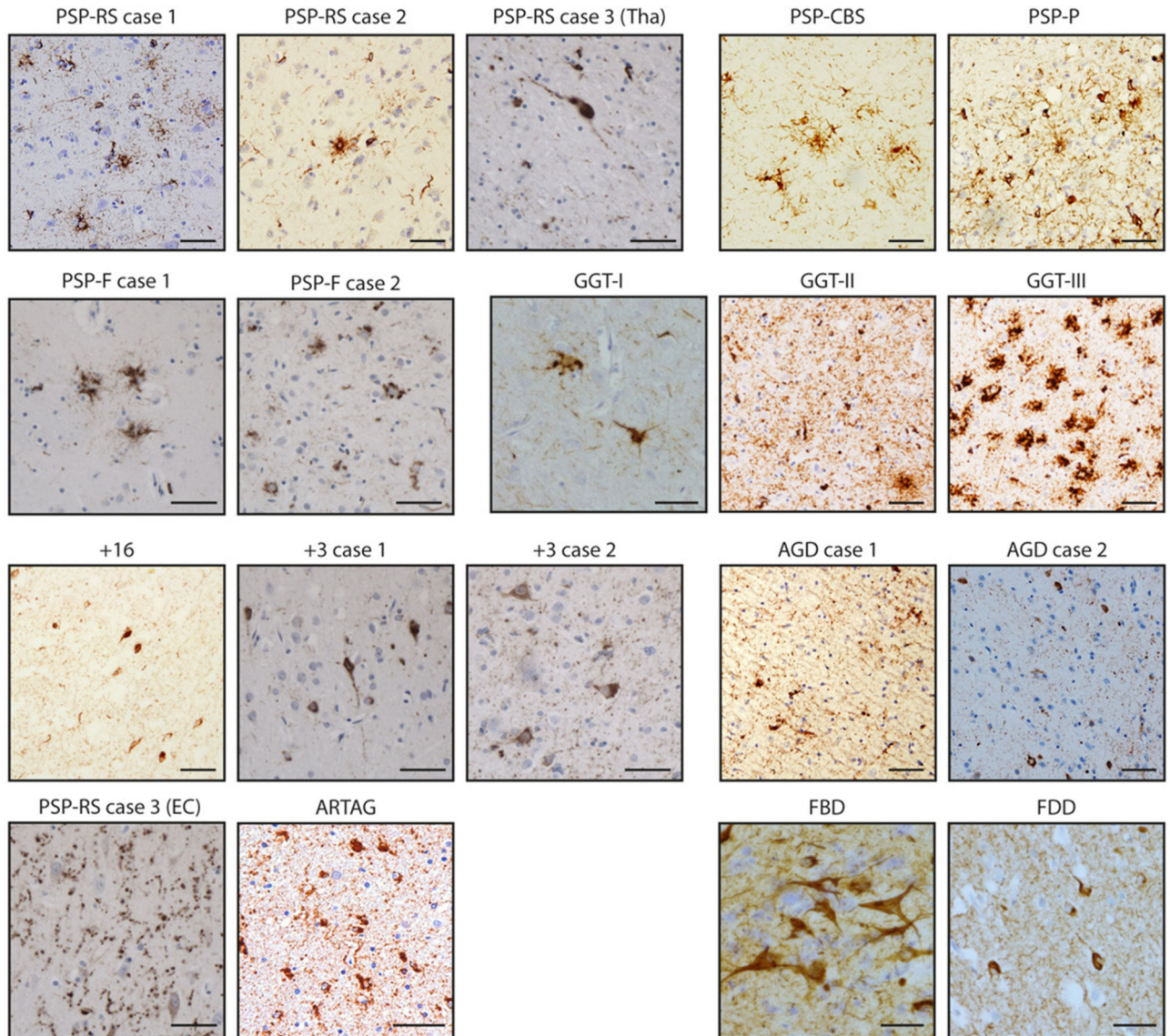


**Extended Data Figure 1. Tau immunohistochemistry**

Representative tau staining of the brain regions used for cryo-EM structure determination (see Methods), using antibody AT8 (pS202/pT205 tau). Scale bars are 50 µm, except for GGT Type I, FBD and FDD, where they are 25 µm. For PSP-RS case 3, both the thalamus (Tha) and the entorhinal cortex (EC) are shown. Similar results were obtained using a minimum of six additional stained sections for each case.
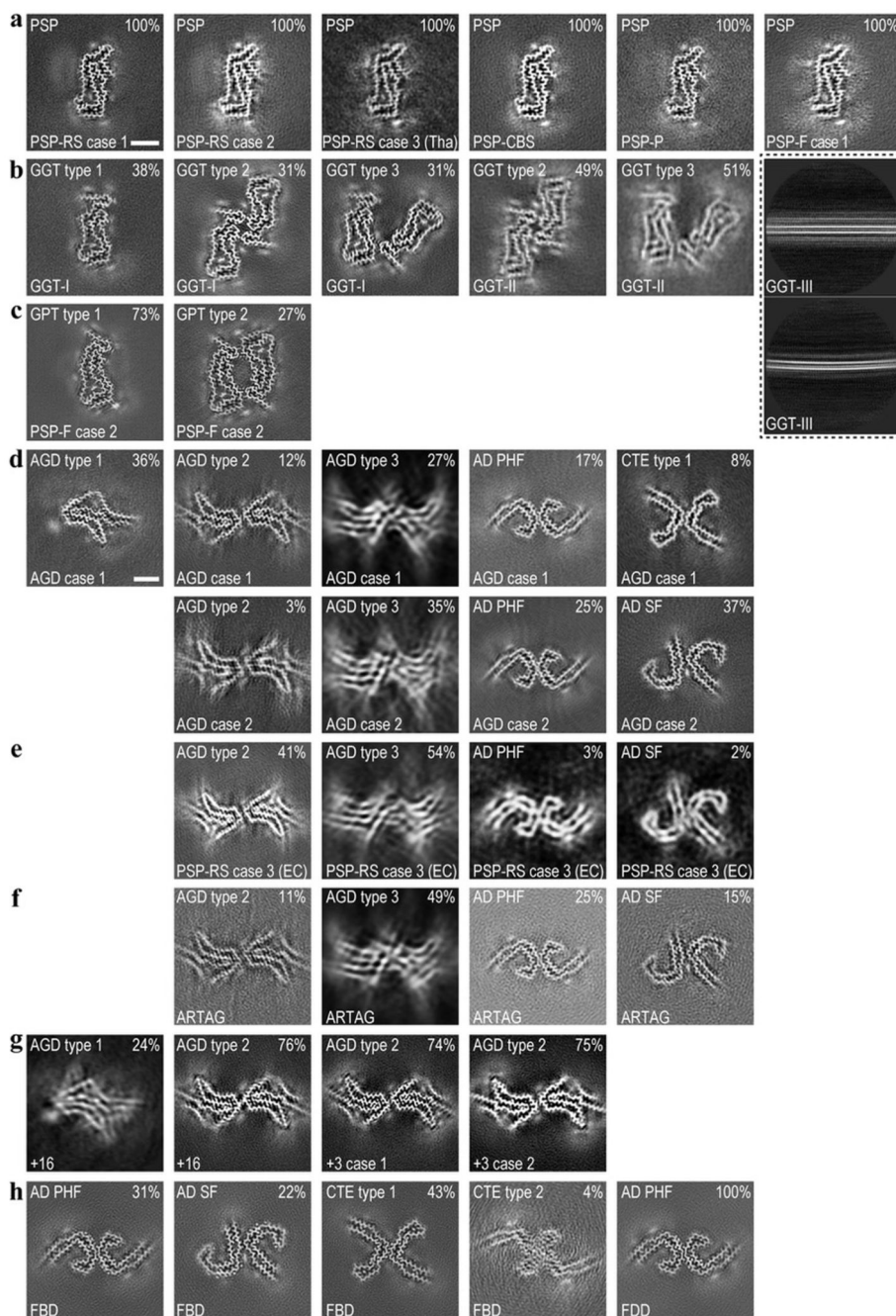
**Extended Data Figure 2. Cryo-EM reconstructions**

**(a)**, Cryo-EM maps for tau filaments from six cases of PSP. For each map, a sum of the reconstructed density for several XY-slices is shown, corresponding to approximately 4.7 Å. The disease cases are referenced at the bottom of each image, the filament types at the top left and the percentages of a given filament type among the tau filaments in the data set at the top right. Scale bar 5 nm. The same scale applies to all panels, except (d-g) **(b-h)**, As in (a), but a case of GGT-I and a case of GGT-II (b); a case diagnosed as PSP-F, but that contains filaments with the PGT fold (c); two cases of AGD (d); scale bar 5nm, the same

scale applies to panels (d-g); entorhinal cortex of case PSP-RS3 (e); a case of ARTAG (f); three cases with mutations +16 or +3 in intron 10 of *MAPT* (g); a case of FBD and a case of FDD (h). Panels (d-f) contain blank squares to indicate the absence of AGD type I filaments in some cases. The inset with dashed lines shows 2D class average images of tau filaments from a case of GGT-III without apparent twist.
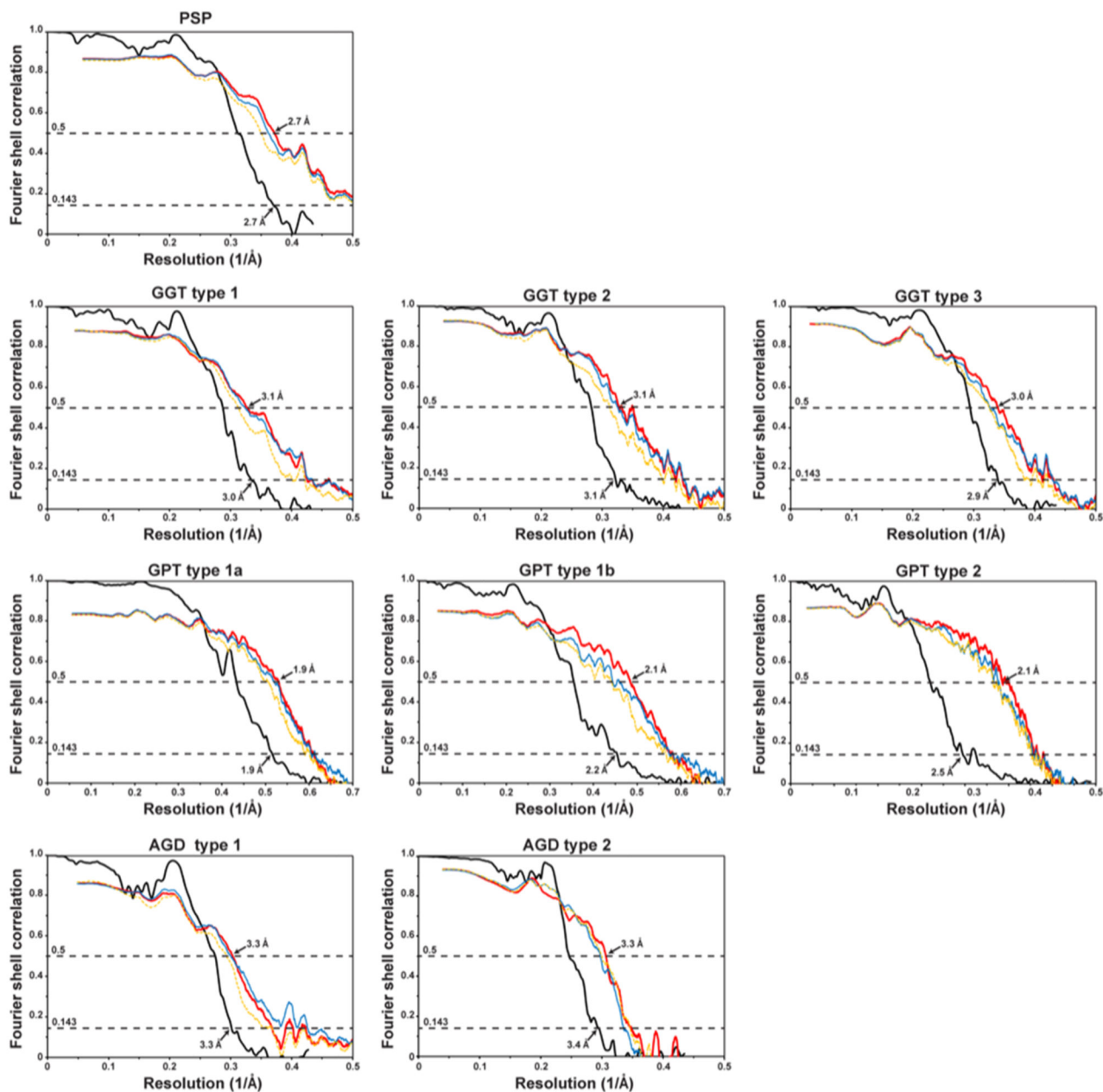
**Extended Data Figure 3. Cryo-EM resolution estimates**
Fourier Shell Correlation (FSC) curves for cryo-EM maps and atomic structures of PSP filaments (from PSP-RS case 1); GGT filament types 1-3 (from GGT-I); GPT filament types

1a, 1b and 2 (from PSP-F case 2); and AGD filament types 1 and 2 (from AGD case 1 and the +16 case, repectively). FSC curves are shown for two independently refined cryo-EM half-maps (black); for the final refined atomic model against the final cryo-EM map (red); for the atomic model refined in the first half-map against that half-map (blue); and for the refined atomic model in the first half-map against the other half-map (yellow).
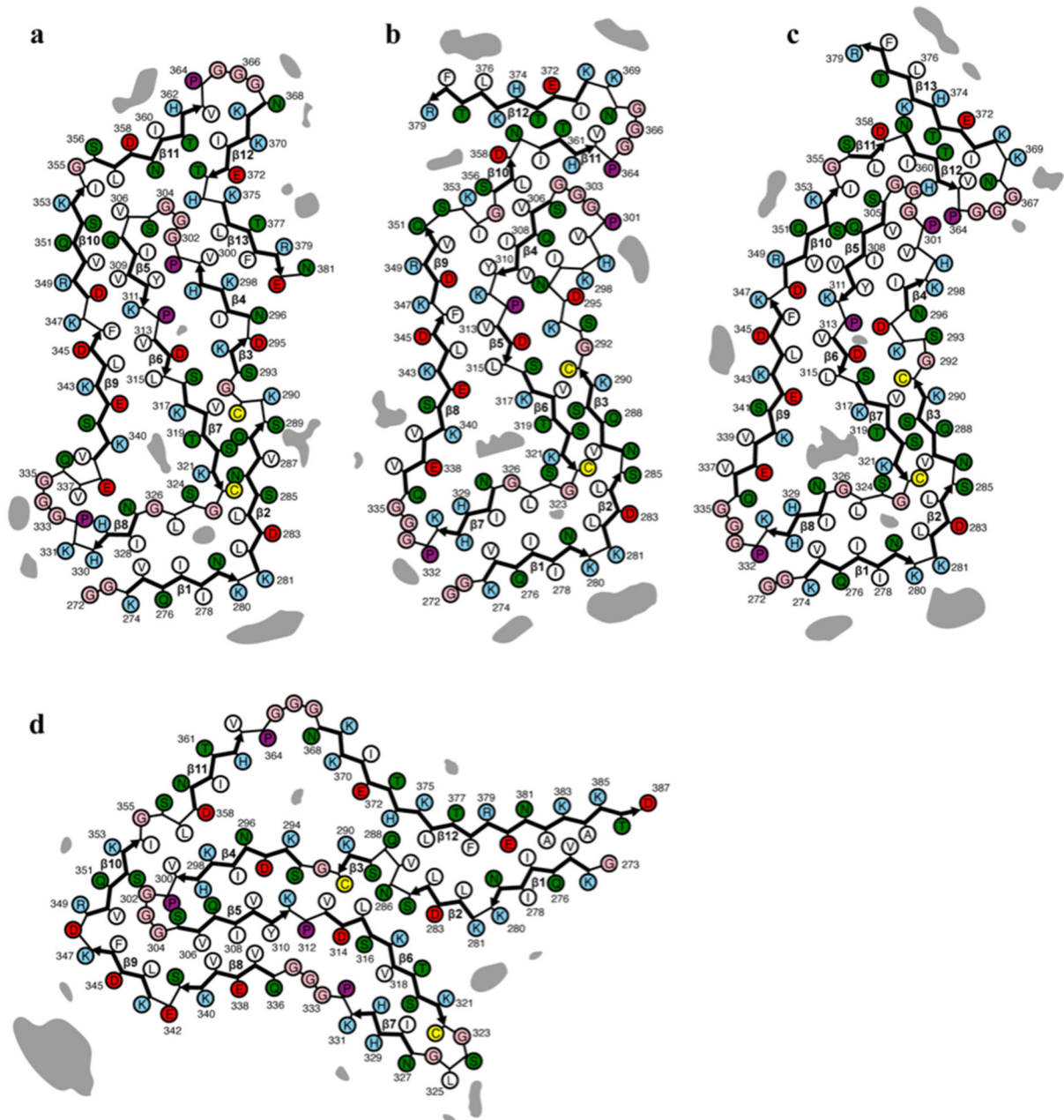


**Extended Data Figure 4. Schematics of tau filament folds**

Schematics of the tau folds for PSP **(a)**, GGT **(b)**, GPT **(c)** and AGD **(d)**. Negatively charged residues are shown in red, positively charged residues in blue, polar residues in green, apolar residues in white, sulfur-containing residues in yellow, prolines in purple and glycines in pink. Thick connecting lines with arrow heads are used to indicate β-strands; additional densities are shown in grey.
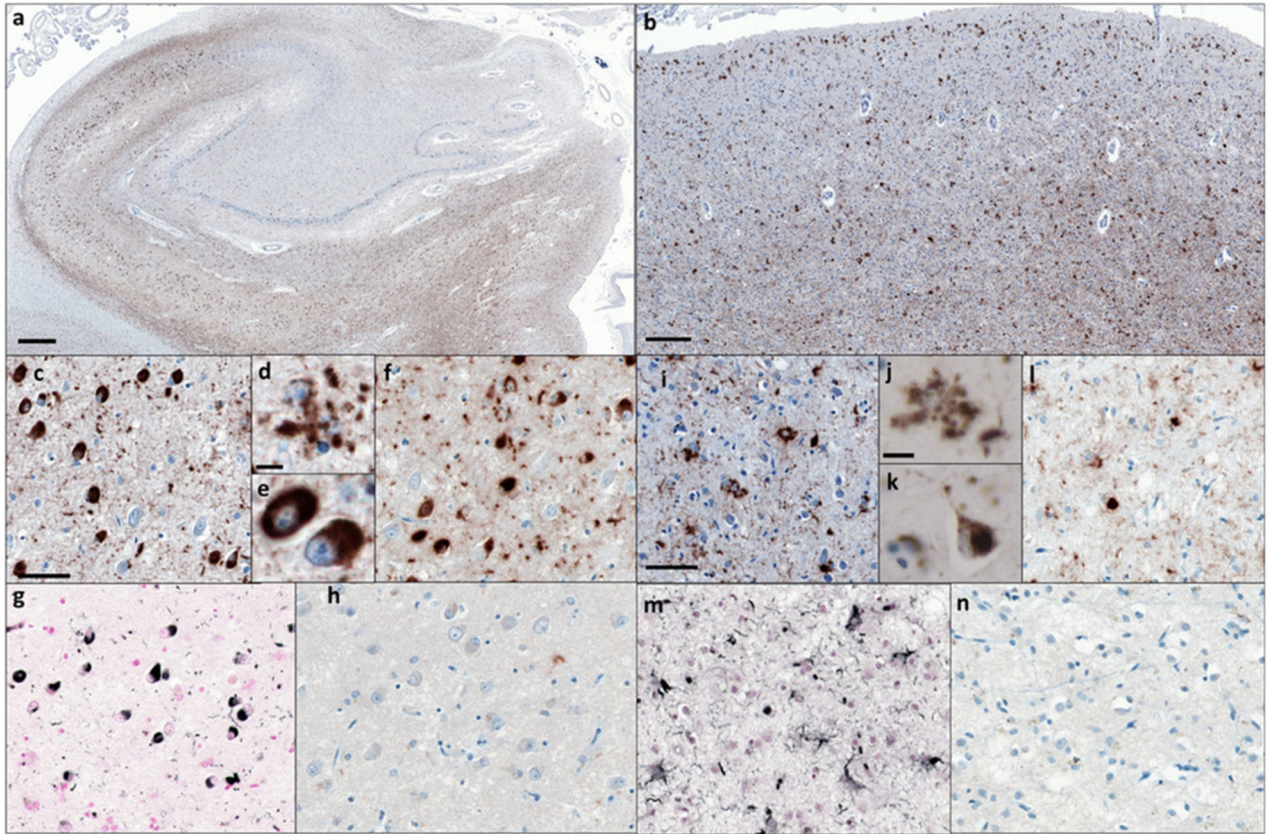


**Extended Data Figure 5. Tau pathology in Limbic-predominant Neuronal inclusion body 4R Tauopathy (LNT, PSP-F case 2)**

**a)** Low power view of hippocampus stained with antibody AT8 (pS202/pT205 tau). **b)** Low power view of frontal cortex stained with AT8. **c)** Higher power view of hippocampus stained with AT8. **d)** AT8-positive globular astrocyte in hippocampus. **e)** AT8-positive neurons in hippocampus. **f)** Hippocampus stained with antibody RD4 (specific for 4R tau). **g)** Gallyas-Braak silver-positive neurons and glial cells in hippocampus. **h)** Hippocampus stained with antibody RD3 (specific for 3R tau). **i)** Higher power view of frontal cortex stained with AT8. **j)** AT8-positive globular astrocyte in frontal cortex. **k)** AT8-positive neurons in frontal cortex. **l)** Frontal cortex stained with RD4. **m)** Gallyas-Braak silver-positive neurons and glial cells in frontal cortex. **n)** Frontal cortex stained with RD3. Representative images are shown. Similar results were obtained using a minimum of six additional stained sections for each panel. Scale bars: 400 μm in (a); 200 μm in (b), 50 μm in (c, f, g, h, i, l, m, n); 10 μm in (d, e, j, k).
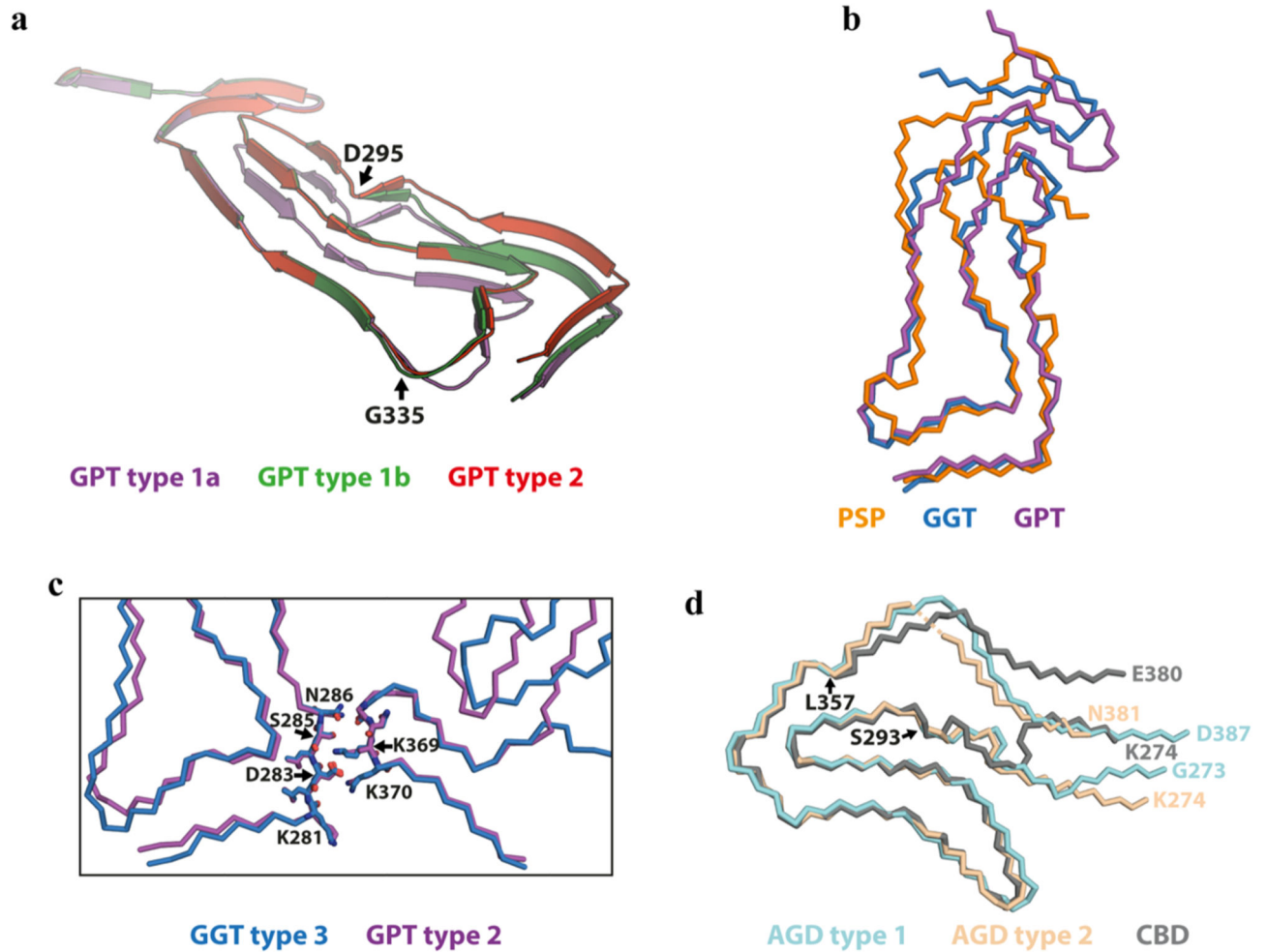
**Extended Data Figure 6. Structural comparisons**

**a)** Comparison of two different main-chain conformations for GPT type 1 filaments (type 1a in purple; type 1b in green) and the main-chain conformation of GPT type 2 filaments (red). **b)** Comparison of the PSP (orange), GGT (blue) and GPT (purple) folds. **c)** Comparison of the inter-protofilament interfaces of GGT type 3 and GPT type 2 filaments. **d)** Comparison of the AGD type 1 (light blue), AGD type 2 (pink) and CBD (grey) folds.
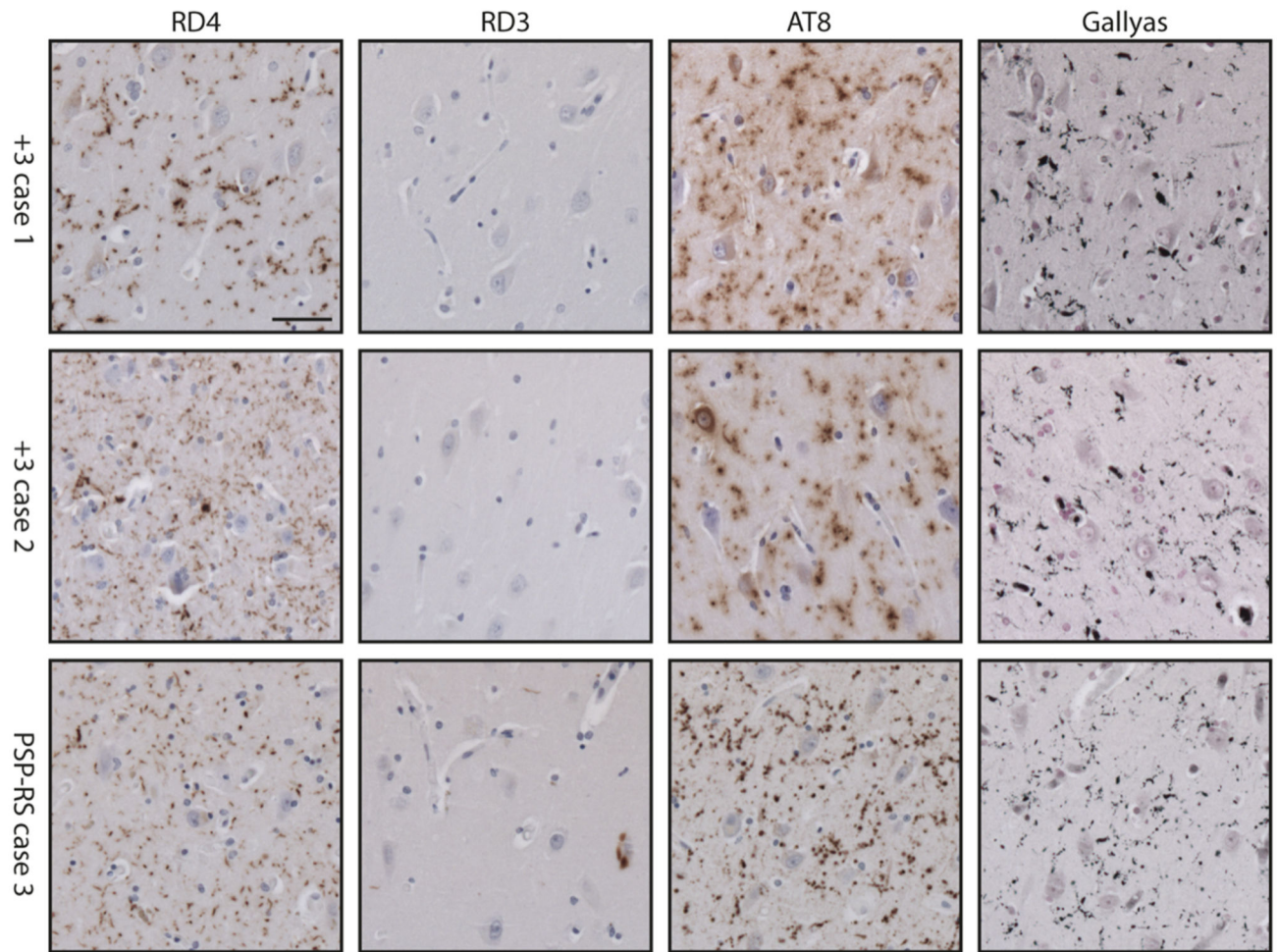
**Extended Data Figure 7. Argyrophilic grains in the entorhinal cortex**
Representative tau staining with antibodies RD4 (4R tau), RD3 (3R tau), AT8 (pS202/pT205 tau), as well as Gallyas-Braak silver, of the entorhinal cortex from cases 1 and 2 with mutation +3 in intron 10 of *MAPT* and from case 3 of PSP-RS. Similar results were obtained using a minimum of six additional stained sections for each case. Scale bar, 50 μm.
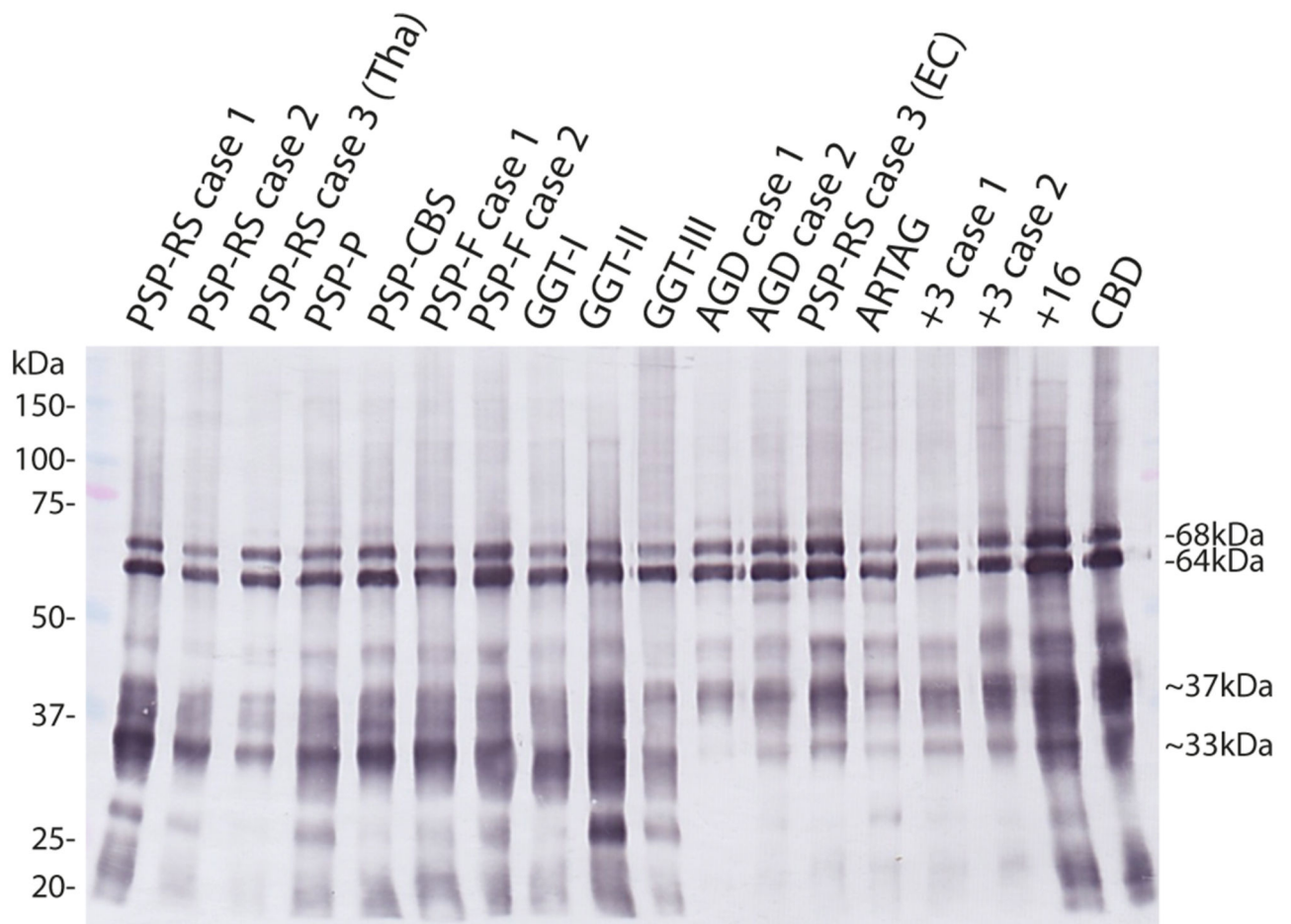
**Extended Data Figure 8. Immunoblot analysis of 4R tauopathies**
Hyperphosphorylated full-length tau (64 and 68 kDa) and C-terminal fragments (33 kDa and 37 kDa) were detected in sarkosyl-insoluble fractions from the brain regions used for cryo-EM by anti-tau antibody T46. A prominent 33 kDa band was characteristic of PSP and GGT; strong 37 kDa bands were in evidence in AGD, ARTAG, cases with intron 10 mutations in *MAPT* (+3 and +16) and in CBD. PSP-RS case 3 had a strong 33 kDa band in thalamus (Tha) and strong 37 kDa bands in entorhinal cortex (EC), consistent with AGD co-pathology. Similar results were obtained in three independent experiments. The original, uncropped image is available in Supplementary Figure 1.

**Extended Data Table 1**
**Cryo-EM data collection, refinement and validation statistics**

|  | PSP-RS case 1 | GGT-I case 1 | PSP-F case 2 | +16 case 1 |
|---|---|---|---|---|
| **Data collection and processing** |  |  |  |  |

| | PSP-RS case 1 | GGT-I case 1 | | | PSP-F case 2 | | | +16 case 1 | |
|---|---|---|---|---|---|---|---|---|---|
| Electron Gun | XFEG | XFEG | | | CFEG | | | XFEG | |
| Detector | K2 | K2 | | | Falcon4 | | | K2 | |
| Energy filter slit width (eV) | 20 | 20 | | | 10 | | | 20 | |
| Voltage (kV) | 300 | 300 | | | 300 | | | 300 | |
| Electron exposure (e–/Å²) | 40 | 50 | | | 50 | | | 54 | |
| Defocus range (μm) | 1.7-2.2 | 1.5-2.5 | | | 0.8-2.0 | | | 1.7-2.8 | |
| Physical pixel size (Å) | 1.15 | 1.15 | | | 0.727 | | | 1.15 | |
| Initial particle images (no.) | 155,030 | 408,018 | | | 630,640 | | | 375,898 | |
| | | type 1 | type 2 | type 3 | type 1a | type 1b | type 2 | type 1 | type 2 |
| Symmetry imposed | C1 | C1 | C1 | C1 | C1 | C1 | C1 | C1 | C2 |
| Final particle images (no.) | 17,316 | 14,873 | 42,381 | 84,438 | 53,363 | 15,096 | 16,813 | 14,582 | 52,134 |
| Map resolution (Å FSC=0.143) | 2.7 | 3.0 | 3.1 | 2.9 | 1.9 | 2.2 | 2.5 | 5.7 | 3.4 |
| Helical rise (Å) | 4.78 | 4.78 | 2.37 | 4.75 | 4.78 | 4.78 | 2.39 | 4.80 | 4.80 |
| Helical twist (°) | -0.86 | -0.75 | 179.65 | -0.73 | -0.36 | -0.39 | 179.82 | -0.36 | -0.40 |
| | PSP-RS case 1 type 1 | GGT-I case 1 type 1 | GGT-I case 1 type 2 | GGT-I case 1 type 3 | PSP-F case 2 type 1a | PSP-F case 2 type 1b | PSP-F case 2 type 2 | AGD case 1 type 1 | +16 case 1 type 2 |
| **Refinement** | | | | | | | | | |
| Initial model used (PDB code) | - | - | - | - | - | - | - | 6TJX | 6TJX |
| Model resolution (Å) | 2.7 | 3.1 | 3.1 | 3.0 | 1.9 | 2.1 | 2.1 | 3.3 | 3.3 |
| FSC threshold | | | | | | | | | |
| Map sharpening *B* factor (Å²) | -12.35 | -18.84 | -34.53 | -29.03 | -18.17 | -20.13 | -23.15 | -37.67 | -35.83 |
| Model composition | | | | | | | | | |
| Non-hydrogen atoms | 4145 | 4060 | 8120 | 8120 | 4166 | 4060 | 8120 | 4340 | 4854 |
| Protein residues | 550 | 540 | 1080 | 1080 | 540 | 540 | 1080 | 575 | 630 |
| Waters | - | - | - | - | 76 | - | - | - | - |
| *B* factors (Å²) | | | | | | | | | |
| Protein | 20.48 | 59.98 | 31.47 | 32.64 | 35.65 | 33.87 | 51.25 | 2.98 | 107.39 |
| Waters | - | - | - | - | 30.00 | - | - | - | - |
| R.m.s. deviations | | | | | | | | | |
| Bond lengths (Å) | 0.004 | 0.004 | 0.007 | 0.006 | 0.004 | 0.004 | 0.005 | 0.003 | 0.009 |
| Bond angles (°) | 0.627 | 0.661 | 1.057 | 0.903 | 0.718 | 0.748 | 0.803 | 0.655 | 1.298 |
| Validation | | | | | | | | | |
| MolProbity score | 1.11 | 1.46 | 1.48 | 1.43 | 1.38 | 1.46 | 1.22 | 1.13 | 1.65 |
| Clashscore | 2.01 | 4.21 | 3.61 | 4.45 | 3.33 | 4.21 | 2.77 | 2.25 | 4.83 |
| Poor rotamers (%) | 0.00 | 0.00 | 0.00 | 0.00 | 0.00 | 0.00 | 0.00 | 0.00 | 0.00 |
| Ramachandran plot | | | | | | | | | |

| | PSP-RS case 1 | GGT-I case 1 | | | PSP-F case 2 | | | +16 case 1 | |
|---|---|---|---|---|---|---|---|---|---|
| Favored (%) | 97.22 | 96.23 | 95.28 | 96.70 | 96.23 | 96.23 | 97.17 | 97.35 | 94.06 |
| Allowed (%) | 2.78 | 3.77 | 4.72 | 3.30 | 3.77 | 3.77 | 2.83 | 2.65 | 5.94 |
| Disallowed (%) | 0.00 | 0.00 | 0.00 | 0.00 | 0.00 | 0.00 | 0.00 | 0.00 | 0.00 |
| PDB | 7P65 | 7P66 | 7P67 | 7P68 | 7P6A | 7P6B | 7P6C | 7P6D | 7P6E |
| EMDB | 13218 | 13219 | 13220 | 13221 | 13223 | 13224 | 13225 | 13226 | 13227 |
| EMPIAR | 10765 | 10766 | | | 10767 | | | 10768 | 10769 |

## Extended Data Table 2
## Cases of tauopathy used for cryo-EM

PSP, progressive supranuclear palsy; GGT, globular glial tauopathy; AGD, argyrophilic grain disease; ARTAG, age-related tau astrogliopathy; MAPT, microtubule-associated protein tau gene; FBD, familial British dementia; FDD, familial Danish dementia.

| Tauopathy | Case number | Gender | Age at death (y) | Brain regions |
|---|---|---|---|---|
| PSP Richardson's syndrome (PSP-RS) | 1 | M | 83 | Frontal cortex |
| | 2 | M | 70 | Frontal cortex |
| | 3 | M | 74 | Thalamus; Entorhinal cortex |
| PSP with a predominant frontal presentation (PSP-F) | 1 | M | 62 | Putamen |
| | 2 | F | 66 | Temporal cortex |
| PSP with predominant parkinsonism (PSP-P) | 1 | M | 63 | Frontal cortex |
| PSP with a predominant presentation of corticobasal syndrome (PSP-CBS) | 1 | F | 88 | Frontal cortex |
| GGT Type I | 1 | F | 77 | Frontal cortex |
| GGT Type II | 1 | F | 76 | Frontal cortex |
| GGT Type III | 1 | M | 62 | Frontal cortex |
| AGD | 1 | M | 90 | Nucleus accumbens |
| | 2 | M | 85 | Nucleus accumbens |
| ARTAG | 1 | F | 85 | Hippocampus |
| *MAPT* intron 10 mutation (+3) | 1 | F | 54 | Frontal cortex |
| | 2 | F | 63 | Frontal cortex |
| *MAPT* intron 10 mutation (+16) | 1 | M | 53 | Frontal cortex |
| FBD | 1 | F | 68 | Hippocampus |
| FDD | 1 | M | 52 | Temporal cortex |

# Supplementary Material

Refer to Web version on PubMed Central for supplementary material.

## Acknowledgements

## Data availability

Cryo-EM maps have been deposited in the Electron Microscopy Data Bank (EMDB) under accession numbers EMD-13218 for PSP, EMD-13219 for GGT type 1, EMD-13220 for GGT type 2, EMD-13221 for GGT type 3, EMD-13223 for GPT type 1a, EMD-13224 for GPT type 1b, EMD-13225 for GPT type 2, EMD-13226 for AGD type 1 and EMD-13227 for AGD type 2. Corresponding refined atomic models have been deposited in the Protein Data Bank (PDB) under accession numbers 7P65 for PSP, 7P66 for GGT type 1, 7P67 for GGT type 2, 7P68 for GGT type 3, 7P6A for GPT type 1a, 7P6B for GPT type 1b, 7P6C for GPT type 2, 7P6D for AGD type 1 and 7P6E for AGD type 2. Cryo-EM data sets have been deposited in the Electron Microscopy Public Image Archive (EMPIAR) under accession numbers 10765 for PSP-RS case 1, 10766 for GGT-I case, 10767 for PSP-F case 2, 10768 for AGD case 1, and 10769 for +16 case. Any other relevant data are available from the corresponding authors upon request.

## References

(1). Fitzpatrick AWP, et al. Cryo-EM structures of tau filaments from Alzheimer's disease. Nature. 547 :185–190. 2017; [PubMed: 28678775]

(2). Falcon B, et al. Tau filaments from multiple cases of sporadic and inherited Alzheimer's disease adopt a common fold. Acta Neuropathol. 126 :699–708.

(3). Falcon B, et al. Structures of filaments from Pick's disease reveal a novel tau protein fold. Nature. 561 :137–140. 2018; [PubMed: 30158706]

(4). Falcon B, et al. Novel tau filament fold in chronic traumatic encephalopathy encloses hydrophobic molecules. Nature. 568 :420–423. 2019; [PubMed: 30894745]

(5). Zhang W, et al. Novel tau filament fold in corticobasal degeneration. Nature. 580 :283–287. 2020; [PubMed: 32050258]

(6). Goedert M, Spillantini MG, Jakes R, Rutherford D, Crowther RA. Multiple isoforms of human microtubule-associated protein tau: Sequences and localization in neurofibrillary tangles of Alzheimer's disease. Neuron. 3 :519–526. 1989; [PubMed: 2484340]

(7). Ghetti B, et al. Frontotemporal dementia caused by microtubule-associated protein tau gene (MAPT) mutations: A chameleon for neuropathology and neuroimaging. Neuropathol Appl Neurobiol. 41 :24–46. 2015; [PubMed: 25556536]

(8). Shi Y, et al. Cryo-EM structures of tau filaments from Alzheimer's disease with PET ligand APN-1607. Acta Neuropathol. 141 :697–708. 2021; [PubMed: 33723967]

(9). Steele JC, Richardson JC, Olszewski J. Progressive supranuclear palsy. A heterogeneous degeneration involving the brainstem, basal ganglia and cerebellum with vertical gaze and pseudobulbar palsy, nuchal dystonia and dementia. Arch Neurol. 10 :333–359. 1964; [PubMed: 14107684]

(10). Williams DR, et al. Characteristics of two distinct clinical phenotypes in pathologically proven progressive supranuclear palsy: Richardson's syndrome and PSP-parkinsonism. Brain. 128 :1247–1258. 2005; [PubMed: 15788542]

(11). Höglinger GU, et al. Clinical diagnosis of progressive supranuclear palsy: The Movement Disorder Society criteria. Mov Disord. 32 :853–864. 2017; [PubMed: 28467028]

(12). Kovacs GG, et al. Distribution patterns of tau pathology in progressive supranuclear palsy. Acta Neuropathol. 140 :99–119. 2020; [PubMed: 32383020]

(13). Sanders DW, et al. Distinct tau prion strains propagate in cells and mice and define different tauopathies. Neuron. 82 :1271–1288. 2014; [PubMed: 24857020]

(14). Molina JA, et al. Primary progressive aphasia with glial cytoplasmic inclusions. Eur Neurol. 40 :71–77. 1998; [PubMed: 9693235]

(15). Ahmed Z, et al. Globular glial tauopathies (GGT) presenting with motor neuron disease or frontotemporal dementia: An emerging group of 4-repeat tauopathies. Acta Neuropathol. 122 :415–428. 2011; [PubMed: 21773886]

(16). Ahmed Z, et al. Globular glial tauopathies (GGT): Consensus recommendations. Acta Neuropathol. 126 :537–544. 2013; [PubMed: 23995422]

(17). Clark CN, et al. Temporal variant frontotemporal dementia is associated with globular glial tauopathy. Cogn Behav Neurol. 28 :92–97. 2015; [PubMed: 26102999]

(18). Tanaka H, et al. Globular glial tauopathy Type II: Clinicopathological study of two autopsy cases. Neuropathology. 39 :111–119. 2019; [PubMed: 30646429]

(19). Fu YJ, et al. Sporadic, four-repeat tauopathy with frontotemporal lobar degeneration, Parkinsonism, and motor neuron disease: a distinct clinicopathological and biochemical disease entity. Acta Neuropathol. 120 :21–32. 2010; [PubMed: 20140439]

(20). Miki Y, Mori F, Hori E, Kaimori M, Wakabayashi K. Hippocampal sclerosis with four repeat tau-positive round inclusions in the dentate gyrus: a new type of four-repeat tauopathy. Acta Neuropathol. 117 :713–718. 2009; [PubMed: 19360425]

(21). Kovacs GG, et al. Tauopathy with hippocampal 4-repeat tau immunoreactive spherical inclusions: a report of three cases. Brain Pathol. 28 :274–283. 2018; [PubMed: 28019685]

(22). Borrego-Écija S, et al. Tauopathy with hippocampal 4-repeat tau immunoreactive spherical inclusions in a patient with PSP. Brain Pathol. 28 :284–286. 2018; [PubMed: 29516660]

(23). Nakane T, et al. Single-particle cryo-EM at atomic resolution. Nature. 587 :152–156. 2020; [PubMed: 33087931]

(24). Braak H, Braak E. Argyrophilic grains: Characteristic pathology of cerebral cortex in cases of adult-onset dementia without Alzheimer changes. Neurosci Lett. 76 :124–127. 1987; [PubMed: 2438598]

(25). Braak H, Braak E. Cortical and subcortical argyrophilic grains characterize a disease associated with adult-onset dementia. Neuropathol Appl Neurobiol. 15 :13–26. 1989; [PubMed: 2471109]

(26). Tolnay M, Clavaguera F. Argyrophilic grain disease: A late-onset dementia with distinctive features among tauopathies. Neuropathology. 24 :269–283. 2004; [PubMed: 15641585]

(27). Saito Y, et al. Staging of argyrophilic grains: an age-associated tauopathy. J Neuropathol Exp Neurol. 63 :911–918. 2004; [PubMed: 15453090]

(28). Ferrer I, Santpere G, Van Leeuwen FW. Argyrophilic grain disease. Brain. 131 :1416–1432. 2008; [PubMed: 18234698]

(29). Kovacs GG, et al. Aging-related tau astrogliopathy (ARTAG): Harmonized evaluation strategy. Acta Neuropathol. 131 :87–102. 2016; [PubMed: 26659578]

(30). Klotz S, et al. Multiple system aging-related tau astrogliopathy with complex proteinopathy in an oligosymptomatic octogenarian. Neuropathology. 41 :72–83. 2021; [PubMed: 33263220]

(31). Spillantini MG, et al. Familial multiple system tauopathy with presenile dementia: A disease with abundant neuronal and glial tau filaments. Proc Natl Acad Sci USA. 94 :4113–4118. 1997; [PubMed: 9108114]

(32). Hutton M, et al. Association of missense and 5'-splice-site mutations in tau with the inherited dementia FTDP-17. Nature. 393 :702–705. 1998; [PubMed: 9641683]

(33). Spillantini MG, et al. Mutation in the tau gene in familial multiple system tauopathy with presenile dementia. Proc Natl Acad Sci USA. 95 :7737–7741. 1998; [PubMed: 9636220]

(34). Forrest SL, et al. Retiring the term FTDP-17 as MAPT mutations are genetic forms of sporadic frontotemporal tauopathies. Brain. 141 :521–534. 2018; [PubMed: 29253099]

(35). Arai T, et al. Identification of amino-terminally cleaved tau fragments that distinguish progressive supranuclear palsy from corticobasal degeneration. Ann Neurol. 55 :72–79. 2004; [PubMed: 14705114]

(36). Taniguchi-Watanabe S, et al. Biochemical classification of tauopathies by immunoblot, protein sequence and mass spectrometric analyses of sarkosyl-insoluble and trypsin-resistant tau. Acta Neuropathol. 131 :267–280. 2016; [PubMed: 26538150]

(37). Miki T, et al. Factors associated with development and distribution of granular/fuzzy astrocytes in neurodegenerative diseases. Brain Pathol. 30 :811–830. 2020; [PubMed: 32293067]

(38). Vidal R, et al. A stop-codon mutation in the BRI gene associated with familial British dementia. Nature. 399 :776–781. 1999; [PubMed: 10391242]

(39). Vidal R, et al. A decamer duplication in the 3' region of the BRI gene originates an amyloid peptide that is associated with dementia in a Danish kindred. Proc Natl Acad Sci USA. 97 :4920–4925. 2000; [PubMed: 10781099]

(40). Holton JL, et al. Regional distribution of amyloid-Bri deposition and its association with neurofibrillary degeneration in familial British dementia. Am J Pathol. 158 :515–526. 2001; [PubMed: 11159188]

(41). Holton JL, et al. Familial Danish dementia: A novel form of cerebral amyloidosis associated with deposition of both amyloid-Dan and amyloid-beta. J Neuropathol Exp Neurol. 2002; 61 :254–267. [PubMed: 11895040]

(42). Dan A, et al. Extensive deamidation at asparagine residue 279 accounts for weak immunoreactivity of tau with RD4 antibody in Alzheimer's disease brain. Acta Neuropathol Commun. 2013; 1 :54. [PubMed: 24252707]

(43). Duyckaerts C, et al. PART is part of Alzheimer disease. Acta Neuropathol. 2015; 129 :749–756. [PubMed: 25628035]

(44). Hallihan GI, et al. Structure of tau filaments in prion protein amyloidoses. Acta Neuropathol. 2021; 142 :227–241. [PubMed: 34128081]

(45). Kametani F, et al. Comparison of common and disease-specific post-translational modifications of pathological tau associated with a wide range of tauopathies. Front Neurosci. 14 581936

(46). Grinberg LT, et al. Argyrophilic grain disease differs from other tauopathies by lacking tau acetylation. Acta Neuropathol. 2013; 125 :581–593. [PubMed: 23371364]

(47). Kovacs GG, et al. MAPT S305I mutation: implications for argyrophilic grain disease. Acta Neuropathol. 2008; 116 :103–118. [PubMed: 18066559]

(48). Rönnbäck A, et al. Neuropathological characterization of two siblings carrying the MAPT S305S mutation demonstrates features resembling argyrophilic grain disease. Acta Neuropathol. 2014; 127 :297–298. [PubMed: 24337498]

(49). Varani L, et al. Structure of tau exon 10 splicing regulatory element RNA and destabilization by mutations of frontotemporal dementia and parkinsonism linked to chromosome 17. Proc Natl Acad Sci USA. 96 :8229–8234. 1999; [PubMed: 10393977]

(50). Poorkaj P, et al. Tau is a candidate gene for chromosome 17 frontotemporal dementia. Ann Neurol. 1998; 43 :815–825. [PubMed: 9629852]

(51). Bugiani O, et al. Frontotemporal dementia and corticobasal degeneration in a family with a P301S mutation in tau. J Neuropathol Exp Neurol. 1999; 58 :667–677. [PubMed: 10374757]

(52). Lladó A, et al. A novel MAPT mutation (P301T) associated with familial frontotemporal dementia. Eur J Neurol. 2007; 14 :e9–e10.

(53). Lewis J, et al. Neurofibrillary tangles, amyotrophy and progressive motor disturbance in mice expressing mutant (P301L) tau protein. Nature Genet. 2000; 25 :402–405. [PubMed: 10932182]

(54). Allen B, et al. Abundant tau filaments and nonapoptotic neurodegeneration in transgenic mice expressing human P301S tau protein. J Neurosci. 2002; 22 :9340–9351. [PubMed: 12417659]

(55). Coughlin DG, Dickson DW, Josephs KA, Litvan I. Progressive supranuclear palsy and corticobasal degeneration. Adv Exp Med Biol. 2021; 1281 :151–176. [PubMed: 33433875]

(56). Josephs KA, et al. Atypical progressive supranuclear palsy with corticospinal tract degeneration. J Neuropathol Exp Neurol. 2006; 65 :396–405. [PubMed: 16691120]

(57). Clavaguera F, et al. Brain homogenates from human tauopathies induce tau inclusions in mouse brain. Proc Natl Acad Sci USA. 2013; 110 :9535–9540. [PubMed: 23690619]

(58). Evans W, et al. The tau *H2* haplotype is almost exclusively Caucasian in origin. Neurosci Lett. 2004; 369 :183–185. [PubMed: 15464261]

(59). Farlow JL, et al. Whole-exome sequencing in familial Parkinson's disease. JAMA Neurol. 2016; 73 :68–75. [PubMed: 26595808]

(60). Spina S, et al. The tauopathy associated with mutation +3 in intron 10 of *Tau*: characterization of the MSTD family. Brain. 2008; 131 :72–89. [PubMed: 18065436]

(61). Braak H, Braak E, Ohm T, Bohl J. Silver impregnation of Alzheimer's neurofibrillary changes counterstained for basophilic material and lipofuscin pigment. Stain Technol. 1988; 69 :197–200.

(62). Guo H, et al. Electron-event representation data enable efficient cryoEM file storage with full preservation of spatial and temporal resolution. IUCrJ. 2020; 7 :860–869.

(63). Zivanov J, et al. A Bayesian approach to beam-induced motion correction in cryo-EM single-particle analysis. IUCrJ. 2020; 6 :5–17.

(64). Rohou A, Grigorieff N. CTFFIND4: Fast and accurate defocus estimation from electron micrographs. J Struct Biol. 192 :216–221.

(65). He S, Scheres SHW. Helical reconstruction in RELION. J Struct Biol. 2017; 198 :163–176. [PubMed: 28193500]

(66). Zivanov J, et al. New tools for automated high-resolution cryo-EM structure determination in RELION-3. eLife. 2018; 7 e42166 [PubMed: 30412051]

(67). Wagner T, et al. SPHIRE-crYOLO is a fast and accurate fully automated particle picker for cryo-EM. Communications Biology. 2019; 2 :218. [PubMed: 31240256]

(68). Scheres SHW. Amyloid structure determination in RELION-3.1. Acta Cryst. 2020; D76 :94–101.

(69). Zivanov J, et al. Estimation of high-order aberrations and anisotropic magnification from cryo-EM data sets in RELION-3.1. IUCrJ. 2020; 7 :253–267.

(70). Chen S, et al. High-resolution noise substitution to measure overfitting and validate resolution in 3D structure determination by single particle electron cryomicroscopy. Ultramicroscopy. 2013; 135 :24–35. [PubMed: 23872039]

(71). Casañal A, et al. Current developments in Coot for macromolecular model building of Electron Cryo-microscopy and Crystallographic Data. Protein Science. 2020; 29 :1069–1078. [PubMed: 31730249]

(72). Williams CJ, et al. MolProbity: More and better reference data for improved all-atom structure validation. Protein Science. 2018; 27 :293–315. [PubMed: 29067766]

(73). Brown A, et al. Tools for macromolecular model building and refinement into electron cryo-microscopy reconstructions. Acta Cryst. D71 :136–153. 2015;

(74). Afonine PV, et al. Real-space refinement in PHENIX for cryo-EM and crystallography. Acta Cryst. 2018; D74 :531–544.

(75). Pettersen EF, et al. UCSF ChimeraX: Structure visualization for researchers, educators, and developers. Protein Sci. 2021; 30 :70–82. [PubMed: 32881101]
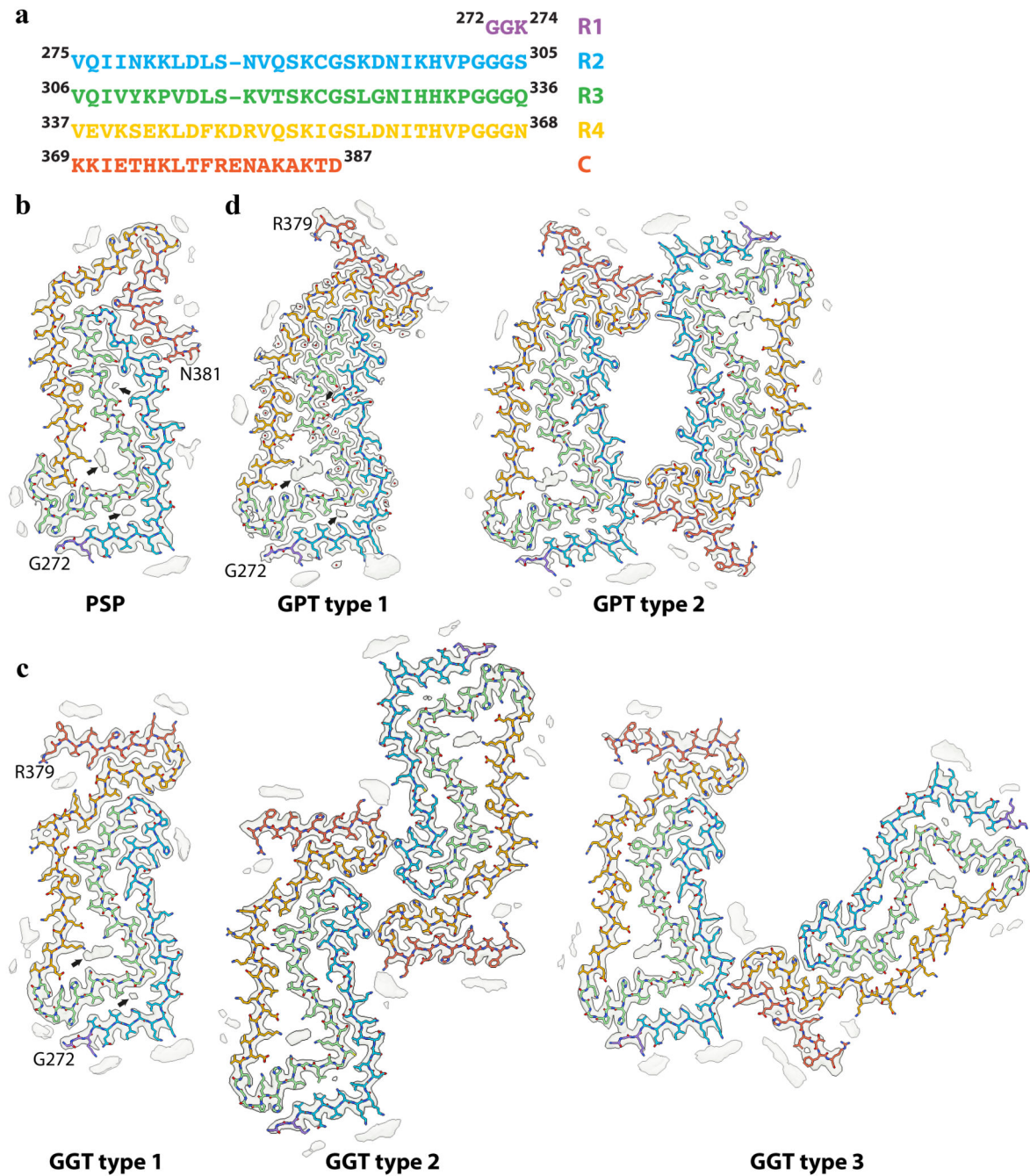
**a**

<sup>272</sup>GGK<sup>274</sup>   R1

<sup>275</sup>VQIINKKLDLS–NVQSKCGSKDNIKHVPGGGS<sup>305</sup>   R2

<sup>306</sup>VQIVYKPVDLS–KVTSKCGSLGNIHHKPGGGQ<sup>336</sup>   R3

<sup>337</sup>VEVKSEKLDFKDRVQSKIGSLDNITHVPGGGN<sup>368</sup>   R4

<sup>369</sup>KKIETHKLTFRENAKAKTD<sup>387</sup>   C

**b**   **d**

PSP    GPT type 1    GPT type 2

**c**

GGT type 1    GGT type 2    GGT type 3

**Figure 1. Three-layered 4R tau filament structures**

(**a**), Amino acid sequence of tau residues 272-387. Residues in R1-4 and in the C-terminal domain are coloured purple, blue, green, gold and orange, respectively; (**b**), Cryo-EM density map (in transparent grey) and atomic model for the PSP filaments. (**c**), As in (b), for GGT type 1, GGT type 2 and GGT type 3 filaments; (**d**) As in (b), for GPT type 1 and GPT type 2 filaments. Black arrows point to additional densities that are described in the main text.
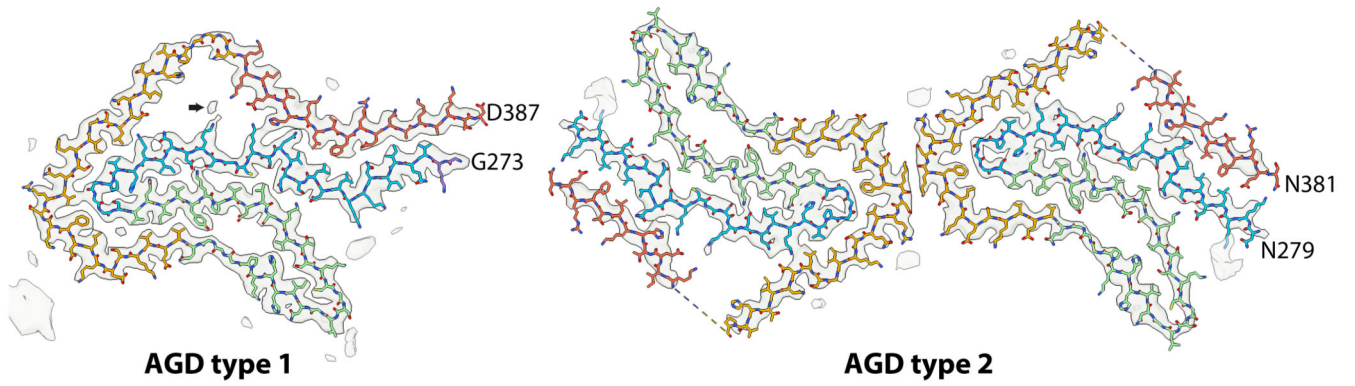
**Figure 2. Four-layered 4R tau filament structures**

Cryo-EM density map and atomic model for AGD type 1 filaments and AGD type 2 filaments. Colours are as in Figure 1. The black arrow points to additional density discussed in the main text. The dotted lines indicate main chain connectivity for which cryo-EM density is missing.
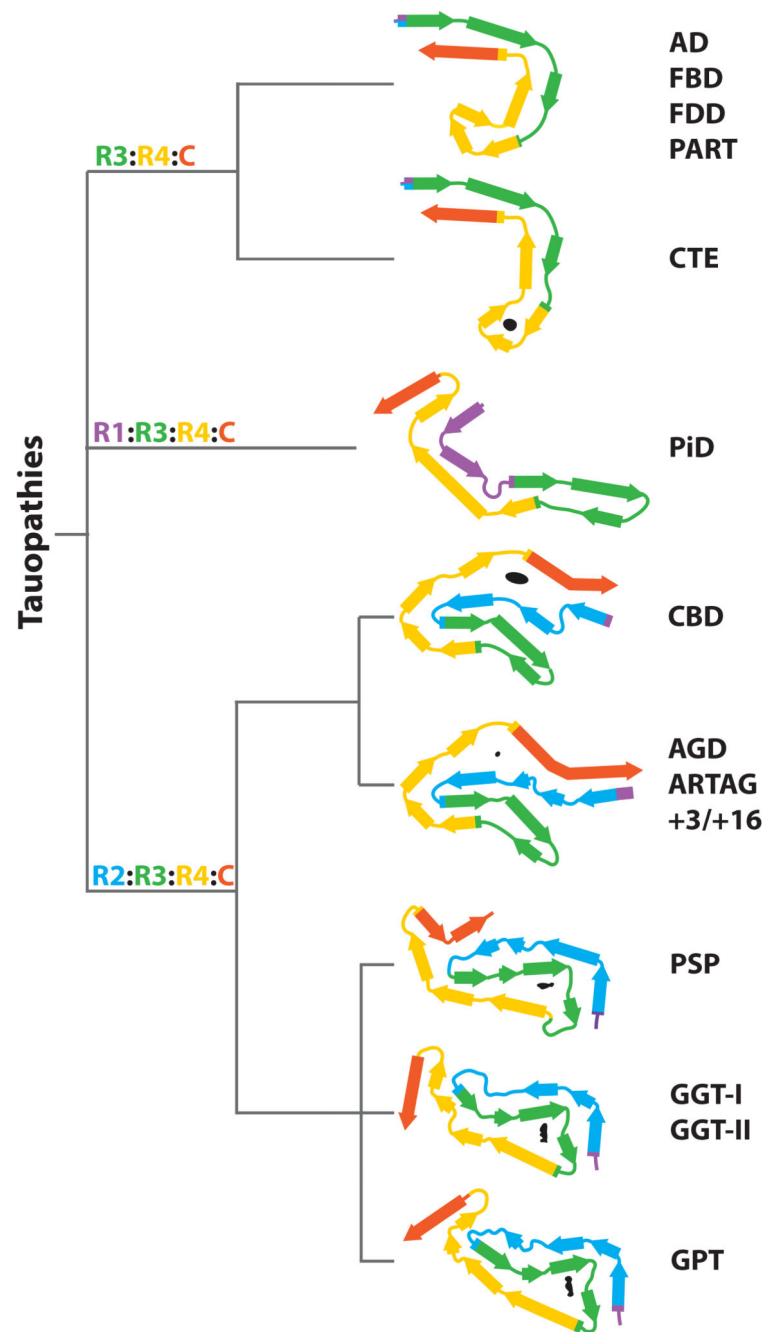
**Figure 3. Structure-based Classification of Tauopathies**
The dendrogram shows the proposed classification of tauopathies as described in the main text, with the corresponding folds displayed with the first β-strand in R3 oriented horizontally, except for the GGT and GPT folds, which are aligned to the PSP fold. Colours are as in Figure 1. Internal, non-proteinaceous densities are shown in black.